Chapter 6

Synthesis, Characterization and Photocalytic Application of Triple Oxide Semiconductor Nanocomposites

Synthesis, Characterization and Photocatalytic Application of Triple Oxide Semiconductor Nanocomposites

6.1. Introduction

Semiconductors are substances with electrical conductivity due to the electron flow intermediate in magnitude between that of a conductor and an insulator. This means conductivity is roughly in the range of 10^3 to 10^{-8} siemens per centimeter. Semiconductor nanocrystals prepared by wet chemical route are often considered for different applications, ranging from light-emitting diodes[1] to biological labels.[2-4] Semiconductor-metal nanocomposites have also been widely employed in photocatalysis. It has been seen that the metal in contact with the semiconductor greatly enhances the overall photocatalytic efficiency.[5] Semiconductor nanocrystals are tiny crystalline particles that exhibit size-dependent optical andelectronic properties.[6-8] Photocatalytic degradation of different organic contaminants by semiconductor photocatalysts has been useful technology for environmental decontamination.[9-11] Semiconductor photocatalysis affords a potential solution to the problems of energy shortages and environmental pollution. Photoefficiency of the bare semiconductor catalyst is limited because of the rapid electron–hole recombination. Therefore, it is urgent to develop highly efficient photocatalytic materials for pollutant degradation. The photocatalytic activity of semiconductor oxide depends on their physical and chemical properties. Because the recombination of photoexcited electrons and holes occurs at crystal lattice defects, crystallinity (i.e., the extent of crystallization) is one of the main factors for photocatalytic reaction efficiency. It is also found that photogenerated charge carriers can be effectively separated inside semiconducting composite materials according to different band gap structures of their components.[12] The main interest arises from the opportunity of tuning the physicochemical properties of semiconductor nanocrystals by simply varying their size due to the effect of quantum confinement.[8,13] Incorporation of metallic and metal oxide nanomaterials to the semiconductor nanoparticles in the continuous solid materials made by the solvothermal methods led to inexpensive photonic materials partly already employed on the market or successfully tested with

respect to numerous applications.[14] The dependence of optical properties on particle size is largely a result of the internal structure of the nanocrystal. However, as the crystal becomes smaller, the number of atoms on the surface increases, which can also impact the optical properties. The atoms on the surface of a crystal facet are incompletely bonded within the crystal lattice and thus, disrupting the crystalline periodicity and leaving one or more "dangling orbital" on each atom pointed outward from the crystal. Band gap tuning is at the core of current materials research and opto-electronic device applications. Through successful tuning of the band gap in semiconductors is difficult, band gap tailored heterostructures, including, 2D electron gas and tunnelling structures have been realised. Such advancements offered a greater understanding of physics regarding quantum electrodynamics and stimulated emergence of many related devices.[15] Moreover, the ability to tune the band gap is becoming increasingly important for developing highly efficient solar cells and transparent conducting oxides. Doped nanomaterials might be a promising owing to their high-specific surface area, low resistances, high catalytic activity, attractive electrochemical and optical properties. These improved physical properties can be ascribed to the various phenomena, like, quantum confinement of electrons, surface disorder etc., that takes place in the nanometer size regime. One of the best ways to enhance the electron–hole separation is to use coupled semiconductors. In coupled semiconductors, a heterojunction interface between the semiconductors of matching band potentials is constructed. In this way, the electric-field-assisted charge transport from one particle to the other via interfaces is favorable for the electron–hole separation in the coupled materials and for the consequent electron or hole abundance on the surfaces of the two semiconductors.[16] Confinement and quantum size effects in nanoparticles induce properties that are significantly different from those of the bulk material as a result of their reduced dimensions.[17] Because of these unique properties, nanomaterials have become a focus of research in modern technology. For example, semiconductor nanoparticles (quantum dots) exhibit discrete energy bands and size-dependent band gap energies; conducting nanoparticles exhibit large optical polarizabilities and nonlinear electrical conductance; and ferromagnetic nanoparticles become superparamagnetic, with size-dependent magnetic susceptibilities.[18,19] Semiconductor co-doped nanomaterials have received significant interest due to their electronic, optoelectronic, magnetic, catalytical, electro-chemical, mechanical behaviors and their potential applications in different research areas. Thus,

semiconductor nanomaterials might be a promising due to their high-specific surface-area, low-resistances, high-catalytic activity, attractive electrochemical and optical properties.[20-24]

In this chapter, we have described the synthesis of Mn_3O_4−ZnO−CdO triple semiconductor nanocomposites by facile wet chemical approach. The as-synthesized metal oxides (*viz.*, Mn_3O_4 and CdO), dual oxides (*viz.*, Mn_3O_4-ZnO, ZnO-CdO and CdO-Mn_3O_4) and triple semiconductor (*viz.*, Mn_3O_4−ZnO−CdO) nanocomposites have been characterized using several spectroscopic and microscopic techniques. It has been found that band gap of the semiconducting particles decreases with increase in hierarchy of the system. Then, the as-synthesized nanocomposites have been exploited for the photocatalytic degradation of Evans blue under ambient condition. Interestingly, it seen that, with increase in hierarchy, the catalytic activity of the semiconducting particles increases and therefore, the reduction in the band gap has been validated.

6.2. Experimental

6.2.1. Synthesis of Metal Oxide Nanoparticles

6.2.1.1. Preparation of Manganese Oxide Nanoparticles

For the preparation of manganese oxide nanoparticles, an amount of 0.0615 g (0.25 mM) of manganese acetate tetrahydrate is taken in a mixture of 20 mL water-ethanol (water : ethanol = 7 : 1) in a double-necked round bottom flask. Then, the mixture was allowed to stir for half an hour for dissolving and after that, 2 mL of 1% trisodium citrate is added along with 2 mL 30% ammonia solution and the volume of the solution is made up to 25 mL. Upon addition of ammonia, color of the solution changes as colorless → faint yellow → dark yellow → dark brown. After 3 h of heating (60-65 °C) of the solution, the heating was stopped but stirring was continued for overnight.

6.2.1.2 Preparation of Cadmium Oxide Nanoparticles

In a typical method, 0.0361 g (0.12 mM) cadmium acetylacetonate is taken in 5 mL of ethanol in a triple-necked round bottom flask. Then, it was allowed to stir along with heating for half an hour. Then, to this dissolved solution, 2 mL of 1% trisodium citrate solution and 30% of 2 mL ammonia solution was added and the volume made up to 25 mL. The solution was distilled at 110–120 ˚C for 2.5 h. After that, heating was

stopped but stirring was continued for overnight. The white dispersion so obtained was washed with ethanol by several times and then, kept in muffle furnace at 300 ˚C for 3 h. After cooling, the yellow powder was collected.

6.2.2. Synthesis of Metal Oxide-Metal Oxide Double Composites

6.2.2.1. Synthesis of Manganese Oxide-Zinc Oxide Nanocomposites To prepare a standard solution of 0.1:1.0 of manganese and zinc precursor, zinc acetate tetrahydrate was dissolved by heating at 45 °C in 7.5 mL ethanol in triple-necked round bottom flask. After about half an hour, manganese oxide nanoparticles were added by dispersing in water. Then, 2 mL 1% trisodium citrate and 2 mL ammonium hydroxide solution was added and the volume was made up to 25 mL. The solution is, then, heated for 2.5 h at 45–65 °C and the stirring was continued for overnight.

6.2.2.2. Synthesis of Manganese oxide-Cadmium oxide Nanocomposites

Finely prepared manganese oxide and cadmium oxide nanoparticles were added together by dispersing in water along with 2 mL of 1% trisodium citrate and 2 mL of 30% ammonium hydroxide solution. The volume of the solution is, then, made up to 25 mL and the solution is then heated and stirred for 2.5 h at 45–65 °C.

6.2.2.3. Synthesis of Zinc oxide-Cadmium Oxide Nanocomposites

Zinc acetate tetrahydrate is dissolved in 7.5 mL methanol and allowed for heating with stirring. After half an hour cadmium oxide nanoparticles was added by dispersing in water. Then, 2 mL sodium citrate and 2 mL ammonium hydroxide was added and the volume was made up to 25 mL. The solution was, then, heated for 2.5 h at 45–65 °C and the stirring was continued for overnight.

6.2.3. Synthesis of Triple Oxide Semiconductor Nanocomposites

In a typical synthesis, manganese oxide and cadmium oxide nanoparticle powders were mixed with dispersed zinc acetate in presence of sodium citrate. Further, 30% ammonium hydroxide was used as reducing agent and the mixture was heated for 2.5 h under stirring condition. A change in colour of the solution at the end of the reaction indicates the formation of the nanocomposites. A schematic presentation of the formation of triple semiconductor nanocomposites in shown in Scheme 6.1.

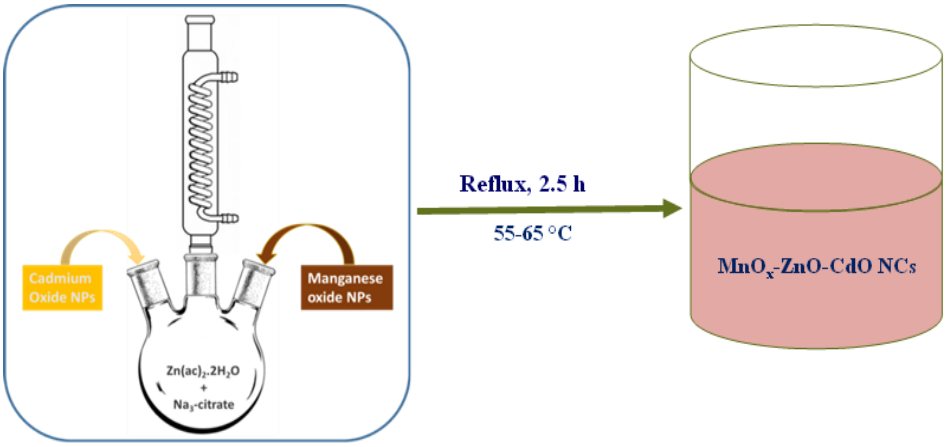

Scheme 6.1. Schematic presentation of typical synthesis of MnO_x-ZnO-CdO semiconductor nanocomposites

6.3. Results and Discussion

In this experiment, triple oxide nanocomposites have been synthesized using three individual semiconductor oxides in a unit system. Typical triple semiconductor nanocomposites have been reported for the first time to the best of our knowledge. These nanostructures have been characterized by absorption spectroscopy, Fourier transform infrared spectroscopy, transmission electron microscopy, high resolution transmission electron microscopy, selected area electron diffraction pattern, energy dispersive X-ray analysis, X-ray diffraction pattern and thermogravimetric analysis.

6.3.1. Absorption Spectroscopy

Fig. 6. 1 shows the absorption spectra of individual, dual and triple oxide

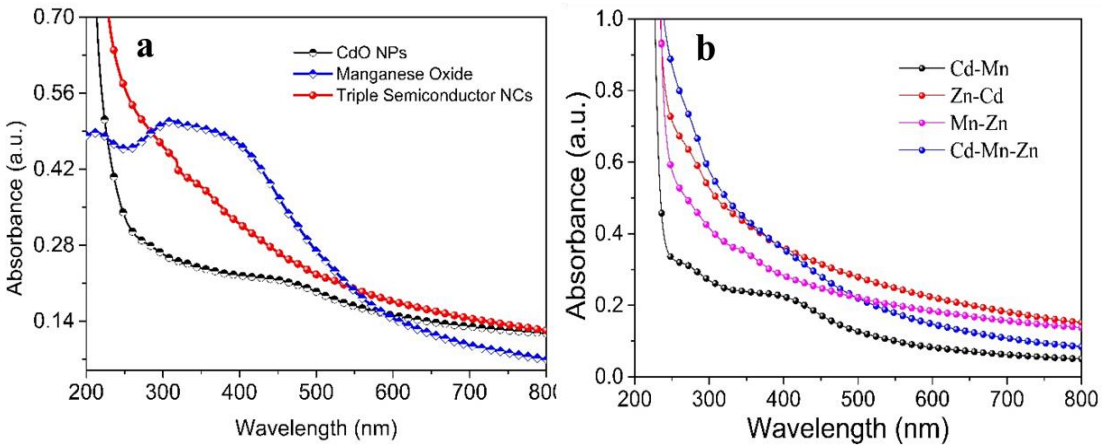

Fig. 6.1. (a) Absorption spectra of (a) individual metal oxide NPs and triple semiconductor NCs and (b) dual and triple oxide semiconductor NCs.

semiconductors. It is seen that nature of individual and dual semiconductors are changed upon formation of triple oxide semiconductors.

6.3.1.1. Theoretical Background of Measurement of Band Gap

Basically, there two types of transitions that can occur at the fundamental edge of crystalline semiconductor**,** direct and indirect transition. Both involve the interaction between electromagnetic wave with an electron in the valance band, which is raised across the fundamental gap to the conduction band. However, indirect transitions also involve simultaneous interaction with lattice vibrations. In crystalline semiconductors, the following equation has been obtained to relate the absorption coefficient to incident photon energy.[25,26]

$$\alpha(\nu)h\nu = B\left(h\nu - E_{gap}\right)^{\mathrm{m}} \qquad (6.1.)$$

where, E_{gap}, B, and hυ are the optical gap, constant, and incident photon energy, respectively; α(ν) is the absorption coefficient. For more precise determination of α, it is necessary to perform corrections to the absorption due to reflection; also, m is the index which can have different values of 1/2, 3/2, 2, and 3.[27]

6.3.1.2. Modification of Band Gap of Dual and Triple Oxide Semiconductors with Variable Composition

We have estimated the optical band gap, E_g, using the Tauc's plot, by the extrapolation of the linear part of the $(\alpha h\nu)^{1/m}$ *vs.* hν curve, where, hν is the incident photon energy. As known from the above relation of absorption coefficient, $\alpha h\nu \sim (h\nu - E_g)^m$, where m = 2 for the indirect and ½ for directly allowed transitions. To determine the possible transitions, $(\alpha h\nu)^{1/m}$ *vs.* $h\nu$ were plotted both for m = 2 and ½ which covers the widest range of data points corresponding to the directly allowed transition. From the $(\alpha h\nu)^2 \sim h\nu - E_g$ plots, the direct band gap values has been estimated. Thus, the modification of the band gap of dual and triple oxide semiconductors have been studied as a function of variable composition as enunciated in Table 6.1.

Table 6.1. Calculated Values of Band Gap for Dual and Triple Oxide Semiconductor Nanocomposites as a Function of Composition

ZnO-MnOx		ZnO-CdO		CdO-MnOx		MnOx-ZnO-CdO		MnOx-ZnO-CdO	
ZnO:MnOx	Band Gap (eV)	ZnO:CdO	Band Gap (eV)	CdO : MnOx	Band Gap (eV)	CdO:ZnO: MnOx	Band Gap (eV)	CdO:ZnO: MnOx	Band Gap (eV)
1.0 : 0.05	2.264	1.0 : 0.05	2.384	1.0 : 0.05	2.179	0.1 : 1.0 : 0.05	2.166	0.05 : 1.0 : 0.1	2.118
1.0 : 0.1	2.311	1.0 : 0.1	2.479	1.0 : 0.1	2.296	0.1 : 1.0 : 0.1	2.295	0.1 : 1.0 : 0.1	2.295
1.0 : 0.5	2.416	1.0 : 0.5	2.516	1.0 : 0.5	2.355	0.1 : 1.0 : 0.5	2.114	0.5 : 1.0 : 0.1	2.307
1.0 : 1.0	2.375	1.0 : 1.0	2.547	1.0 : 1.0	2.394	0.1 : 1.0 : 1.0	2.251	1.0 : 1.0 : 0.1	2.451
1.0 : 2.0	2.511	1.0 : 2.0	2.606	1.0 : 2.0	2.467	0.1 : 1.0 : 2.0	2.228	2.0: 1.0 : 0.1	2.622

6.3.2. FTIR Spectroscopy

Fig. 6.2 shows the FTIR spectra of cadmium oxide nanoparticles, manganese oxide nanoparticle and triple oxide semiconductor nanocomposites. In case of both cadmium oxide and manganese oxide nanoparticles, one M–O stretching frequency peak is observed at 729 cm^{-1}, but in case of triple oxide semiconductor, the peak is shifted towards lower region at around 725 cm^{-1}. Another evidence of triple semiconductor formation is the shifting peak at around 520 cm^{-1} in triple semiconductor while it appears at 524 cm^{-1} in case manganese oxide.[28] In addition, the separation twin peak at 806 cm^{-1} is clear evidence for triple oxide semiconductor system, while it appears as a unique peak in metal oxide nanoparticles.[29,30]

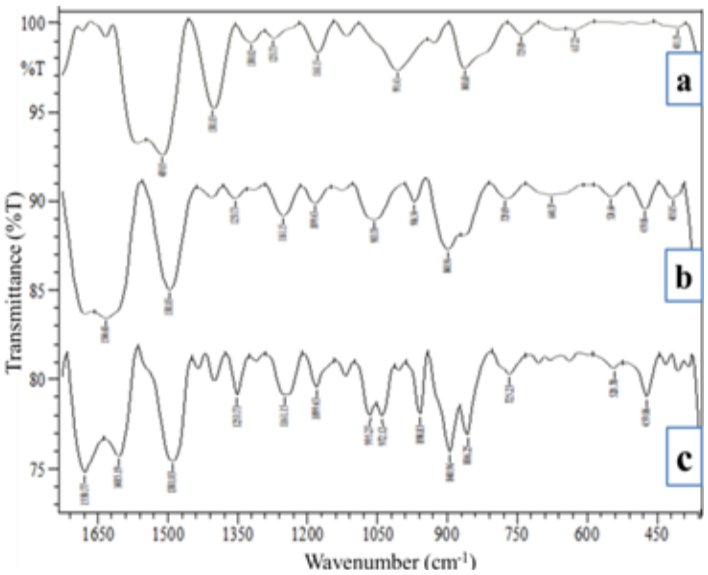

Fig.6.2. Fourier tansform infrared spectra of (a) cadmium oxide, (b) manganese oxide and (c) triple oxide semiconductor nanocomposites.

6.3.3. Morphology and Crystallinity of the Mn_3O_4 NPs, CdO NPs, and Mn_3O_4–ZnO–CdO NCs

The morphology and crystallinity of the individual components and their nanocomposites have been characterized by transmission electron microscopy, high resolution transmission electron microscopy and selected area electron diffraction

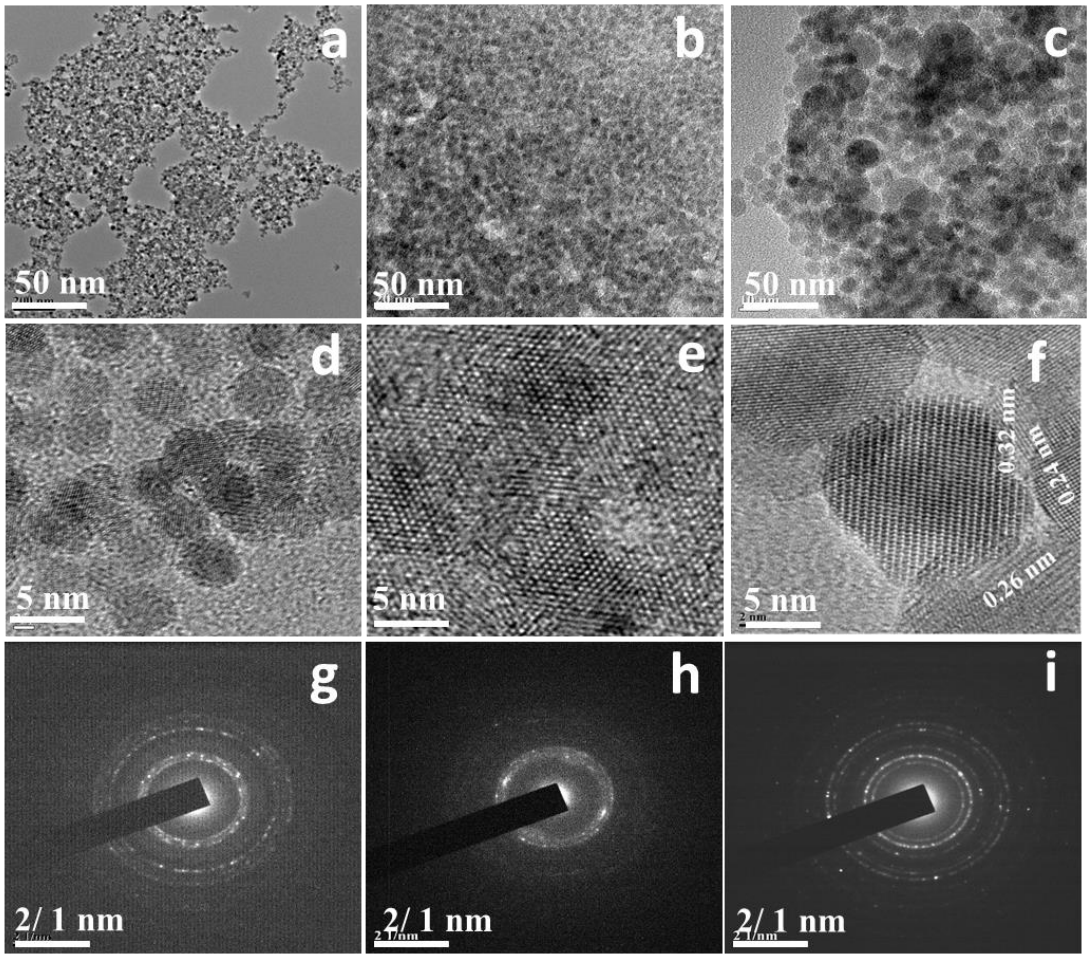

Fig.6.3. (a, b, c) TEM images of Mn_3O_4, CdO NPs and (Mn_3O_4-ZnO-CdO) NCs respectively; (d, e, f) HRTEM images of of Mn_3O_4, CdO NPs and (Mn_3O_4-ZnO-CdO) NCs respectively; and (g, h and i) SEAD patterns of Mn_3O_4, CdO nanoparticles and the corresponding (Mn_3O_4-ZnO-CdO) nanocomposites, respectively.

(SAED) pattern as shown in Fig. 6.3. Representative transmission electron micrographs of Mn_3O_4 (panel a), CdO (panel b) and Mn_3O_4-ZnO-CdO (panel c) show that the particles are tetragonal with average average diameter 6±2, 5±2 nm and 12±3, respectively. High resolution transmission electron micrograph Mn_3O_4 (panel d), CdO nanoparticles (panel e) showing the corresponding lattice spacings between the fringes is about 0.24 nm which corresponds to the distance between the (211) planes of the Mn_3O_4 tetragonal crystal lattice[31] and 0.32 nm that could be assigned to the

(111) planes of CdO orientations of the single phase cubic monteponite crystal lattice.[24] The HRTEM image of Mn_3O_4-ZnO-CdO nanocomposites (panel f) displaying the distinct interplanar distance between the fringes is about 0.24 nm which corresponds to the distance between the (211) planes of the Mn_3O_4 tetragonal crystal lattice,[31] 0.32 nm that could be assigned to the (111) planes of CdO orientations of the single phase cubic monteponite crystal lattice[24] and 0.26 corresponding (100) lattice plane of ZnO wurtzite[32] authenticating the formation of Mn_3O_4-ZnO-CdO nanocomposites. Selected area electron diffraction pattern of the Mn_3O_4 particles (panel g) is consistent with tetragonal Mn_3O_4 with strong ring patterns due to (101), (103) and (220) planes and therefore, confirms thecrystallinity of the particles.[33] The ring pattern (panel h) can be indexed as (111), (200), (220), (311), (222) and (400) corresponding to reticular orientations of the single phase cubic monteponite CdO structure.[24] The selected area electron diffraction pattern (panel i) of the Mn_3O_4 particles, CdO particle and additional evolution of ZnO with strong ring patterns to reveal the appearance of polycrystalline-like diffraction, which are consistent with reflections (100), (002), (101), (102) and (110), corresponding to the hexagonal wurtzite phase of ZnO particles. The appearance of diffraction peaks corresponding to Mn_3O_4-ZnO-CdO, indicates the crystallinity of triple oxide semiconductor nanocomposites.[34]

6.3.4. X-ray Diffraction Pattern of Mn_3O_4-ZnO-CdO Nanocomposites

For the structural characterization of as-synthesized materials, powder X-ray diffraction pattern of Mn_3O_4-ZnO-CdO nanocomposites is shown in Fig 6.4. All diffraction peaks of trace a implying a crystalline structure can be indexed to the tetragonal structure with space group $I4_{I/amd}$, which are consistent with the standard values of bulk Mn_3O_4 (JCPDS# 24-0734).[35]Along with, the diffraction peaks at can be indexed as (111), (200), (220) and (311) to the single phase cubic monteponite CdO structure (JCPDS# 05-0640).[36] The remaining diffraction peaks with comparatively high intensities can be indexed as (100), (102), (103) and (112) corresponding to the hexagonal wurtzite phase of ZnO particles. The co-existence of Mn_3O_4, CdO and ZnO peaks in the diffraction pattern provide clear evidence of the formation of MnO_4-ZnO-CdO nanocomposites.[34]

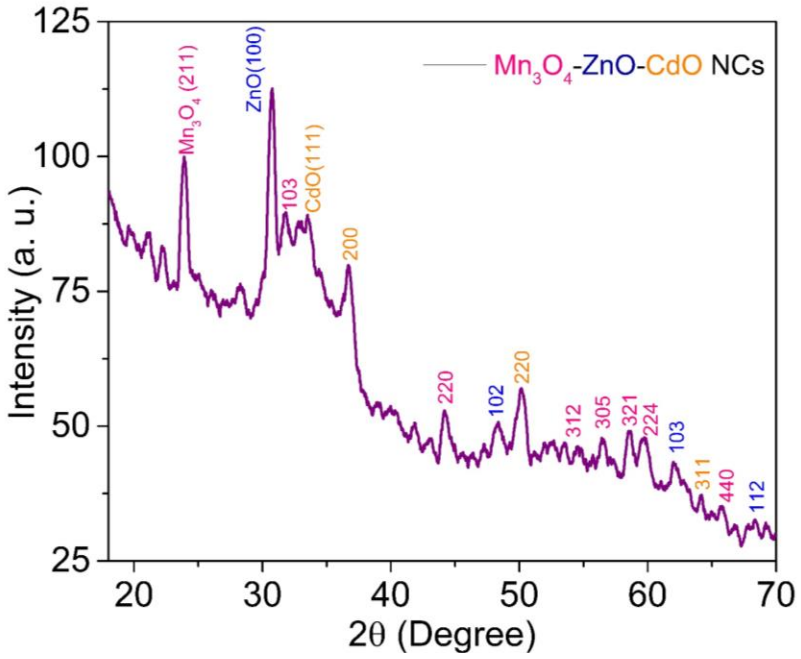

Fig.6.4 X-ray diffraction pattern of Mn_3O_4-CdO-ZnO nanocomposites

6.3.5. Thermogravimetric Analysis and Energy Disperse X-ray Diffraction Pattern of Mn_3O_4-ZnO-CdO Nanocomposites

Thermogravimetric analysis and energy disperse X-ray diffraction pattern of the as-dried powder sample of Mn_3O_4-ZnO-CdO nanocomposites are shown in Fig.6.5. TGA curve shows three weight loss steps in the curve: 5.43 wt% loss corresponding to the water desorption (up to 200 °C). The following major weight losses (11.06 wt%) and (16.66 wt%) in the temperature range of 250-480 °C are corresponding to

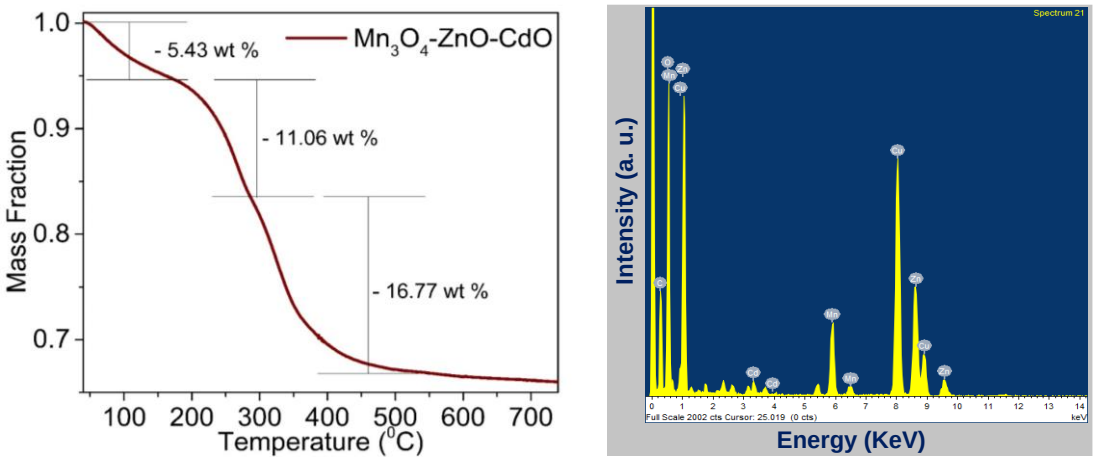

Fig. 6.5 (left) TGA weight loss pattern and (right) energy dispersive X-ray spectrum of the as-synthesized Mn_3O_4–ZnO–CdO triple NCs.

the decomposition of citrate and acetate counter ions, responsible for the stabilisation of the nanocomposites.[37,38] Representative energy dispersive X-ray spectrum of Mn_3O_4-ZnO-CdO triple semiconductor nanocomposites, which reveals that the particles are composed of Mn, Cd, Zn and O elements; the appearance of Cu is from the carbon-coated copper TEM grid.

6.3.6. Photocatalytic Degradation of Evans Blue by Mn_3O_4-ZnO-CdO NCs under Visible Light Irradiation

In comparison with bulk semiconductors, nanocrystals have a diverse and growing range of parameters that can modulate their electronic band gaps, including, size, shape, and composition.[39,40] To probe the modification of band gap in dual and triple oxide semiconductor system, we have performed photocatalytic degradation of Evans blue dye in presence of visible light. Photocatalysis where photons are used for catalytically activating chemical reactions on the surface of photosensitised catalysts, remains one of the leading hubs of research for harvesting the solar light. Typically, photocatalysts generate the charge carriers on excitation and under suitable conditions, these are transferred from the catalysts to the reaction medium, which, in turn, initiate the chemical reaction.[41] It has now, commonly, been experienced that small transition metal clusters exhibit their chemical behavior as photocatalysts. Nevertheless, ZnO has received strong attention as promising photocatalyst due to its innocuousness, abundance, facile synthesis allowing for versatile shapes and sizes,

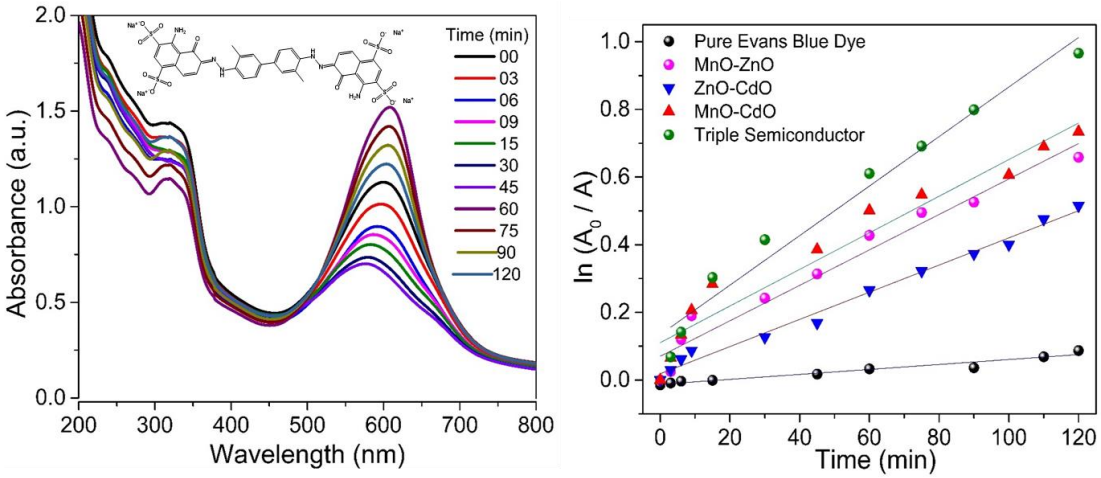

Fig. 6.6 (left) Absorption spectral changes during the degradation of Evans blue (20 μM) in the presence of Mn_3O_4-ZnO-CdO triple semiconductor NCs (33 μg) upon visible light irradiation; (right) profile showing the plot of $ln(A_0/A)$ as a function of time for photocatalytic degradation of Evans blue in the presence of Mn_3O_4 –ZnO, Mn_3O_4–CdO, ZnO-CdO and Mn_3O_4–ZnO-CdO NCs.

and its easy surface modification.[42] But the major drawback for exploiting their utility under visible light irradiation is that the optical absorption of these materials lies in the UV range of the solar spectrum due to the wide band gaps of more than 3.0 eV so that only a small part of the incident energy can be converted. However, this issue can be improved, significantly, by mixing zinc oxide semiconductor with manganese oxide and cadmium oxide nanostructures mixing altogether to form typical triple oxide semiconductor nanocomposites system. Now, the catalytic activities of the triple oxide semiconductor nanocomposites have been tested for photochemical decomposition of Evans blue under visible light illuminations as the model reaction. Evans blue [Tetrasodium (6*E*,6'*E*)-6,6-{(3,3'-dimethylbiphenyl-4,4'-diyl)di(1*E*)hydrazin-2-yl-1-ylidene}bis(4-amino-5-oxo-5,6 dihydronaphthalene-1,3-disulfonate)], also known as 'Direct Blue 53', is a diazo dye and can be useful in physiology in estimating the proportion of body water contained in blood plasma.[43] Furthermore, they are used for colouring of rayon, paper, leather and to a less extent nylon; however, discharge of such colourants to surface water cause harmful environmental effects.

The photocatalytic degradation of Evans blue was employed as the model reaction as its degradation can, easily and quantitatively, be monitored via its absorption spectroscopy (Fig. 6.6). Moreover, Evans blue was chosen because of its high stability against spontaneous photobleaching in the absence of a photocatalyst. In the photocatalytic reaction, 33 μg of the as-prepared catalysts was dispersed with 3.0 mL of 20 μM aqueous solution of the dye molecules and the dispersion was stirred in the dark for 2 h to reach adsorption-desorption equilibrium between the catalysts and dye molecules. Then, the solution was irradiated with the tungsten lamp and the progress of the reaction was followed in the absorption spectrophotometer (left panel). The blank of the instrument was performed before addition of Evans blue. Aqueous solution of the dye molecules exhibit a very intense absorbance band centered around 608 nm corresponding to $n \rightarrow \pi^*$ transitions and molar extinction coefficient, $\varepsilon \sim 7.8 \times 10^4$ M^{-1} cm^{-1} corresponding to the monomeric form of the dye.[43] As controls, an aqueous solution of EB (3.0 ml, 20 μM) was exposed to the same tungsten lamp under identical experimental conditions. It was observed that, in the absence of the catalysts, the photochemical decomposition of the dye is not appreciable in the experimental time scale. In addition, it was noted that the decomposition of the dye is also very slow in the presence of pure manganese oxide or cadmium oxide; however, the

degradation becomes moderately faster in the presence of dual oxide nanocomposites and degradation becomes promisingly faster in the presence triple oxide nanocomposites. These changes in the absorption spectral features indicate that with increase in irradiation time Evans blue undergoes photocatalytic degradation and forms small fragmented organic products.[44]The decrease in intensity of the absorption band of Evans blue at 608 nm has been used to access the photocatalytic activity of the nanostructures for the degradation of the dye. A profile showing the plot of $\ln(A_0/A)$ where, A_0 is the absorbance at t = 0 and A the absorbance at time t = t, as a function of time as presented (right panel) shows that the reaction follows first order kinetics and the corresponding catalytic rate constants (K_{cat}) have been calculated as 0.7×10^{-3}, 4.0×10^{-3}, 5.24×10^{-3}, 5.41×10^{-3}, and 7.32×10^{-3} min^{-1} in the presence of pure EB without catalyst and ZnO-CdO, Mn_3O_4-ZnO, Mn_3O_4-CdO and Mn_3O_4-ZnO-CdO nanocomposite systems. Thus, the design of triple semiconductor metal oxide nanocomposites exhibit better photocatalytic activity in comparison with dual oxide semiconductors.

6.3.7. Reusability of the Mn_3O_4-ZnO-CdO Catalysts

The reusability of Mn_3O_4-ZnO-CdO catalysts was tested for the degradation of Evans blue dye under identical reaction conditions. After complete degradation, the catalyst was separated and washed with a large amount of deionized water; then, the catalyst was washed with methanol and filtered. The recovered catalyst was dried in a hot air oven at 100 °C for 90 min and used for second run. Similarly, next four successive runs were performed and the catalysts were found to be active without any significant loss of activity up to six cycles of operation.

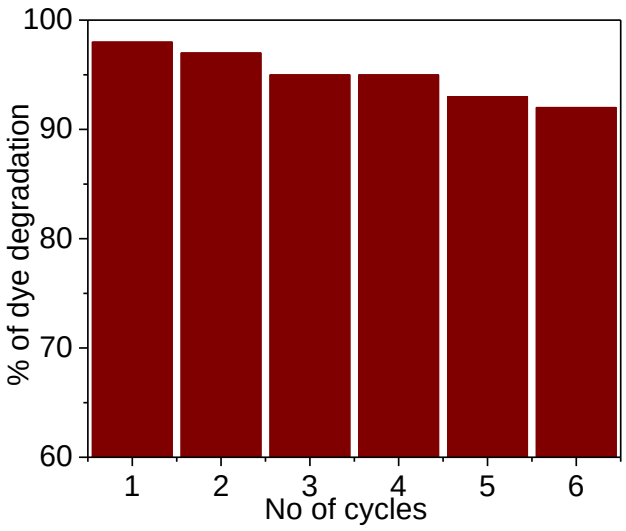

Fig. 6.7. Histogram showing the percentage of the degradation of the dye in each cycle.

6.4. Conclusion

In conclusion, double and triple oxide semiconductor nanocomposites have been synthesized under facile hydrothermal conditions. The as-synthesized nanocomposites have been characterized by varieties of spectroscopic and microscopic techniques. Using the Tauc's model, the absorption spectrum fitting method has been employed to estimate the optical band gap. It has been seen that the band gap of the semiconducting particles becomes modified upon conjugation and reduced with increasing number of metal oxides in the composites. The reduction in the band gap of the nanocomposites has been probed by employing the nanocomposites towards the photocatalytic degradation of Evans blue under visible light irradiation. Lastly, the simple and facile approach of the present strategy builds a good platform towards fabricating other semiconductor assemblies over a wide range of material combinations with morphological anisotropy and functional diversities.

6.5. References

1. V. L. Colvin, M. C. Schlamp and A. P. Alivisatos, *Nature,* 1994, **370,** 354–357.
2. M. Bruchez, M. Moronne, P. Gin, S. Weiss and A. P. Alivisatos, *Science,* 1998, **281,** 2013–2019.
3. W. C. W. Chan and S. Nie, *Science,* 1998, **281,** 2016–2024.
4. G. P. Mitchell, C. A. Mirkin and R. L. Letsinger, *J. Am. Chem. Soc.,* 1999, **121**, 8122–8123.
5. T. K. George and P. V. Kamat, *Acc. Chem. Res.*, 2003, **36,** 888–898.
6. L. E. Brus, *J. Chem. Phys.,* 1984, **80**, 4403–4409.
7. M. G. Bawendi, M. L. Steigerwald and L. E. Brus, *Annu. Rev. Phys. Chem.,* 1990, **41**, 477– 496.
8. A. P. Alivisatos, *J. Phys. Chem.,* 1996, **100**, 13226–13239.
9. A. Kudo, K. Omori and H. Kato, *J. Am. Chem. Soc.,* 1999, **121**, 1145−1155.
10. R. Asahi, T. Morikawa, T. Ohwaki, K. Aoki and Y. Taga, *Science,* 2001, **293**, 269−271.
11. Z. G. Zou, J. H. Ye, K. Sayama and H. Arakawa, *Nature*, 2001, **414**, 625−627.
12. D. J. Yang, H. W. Liu, Z. F. Zheng, Y. Yuan, J. C. Zhao, E. R. Waclawik, W. B. Ke and H. Y. Zhu, *J. Am. Chem. Soc*., 2009, **131**, 17885−17893.
13. H. Weller, *Angew. Chem., Int. Ed*., 1993, **32,** 41.

14. C. Rottman, G. Grader, Y. D. Hazan, S. Melchior and D. Avnir, *J. Am. Chem. Soc.*, 1999, **121**, 8533–8543.
15. F. Capasso, *Science*, 1987, **235**, 172–176.
16. X. Lin, J. Xing, W. Wang, Z. Shan, F. Xu and F. Huang, F. *J. Phys. Chem. C*, 2007, **111**, 18288−18293.
17. K. V. P. M, Shafi, A. Ulman, X. Yan, N. L. Yang, Estournes, H. White and M. Rafailovich, *Langmuir*, 2001, **17**, 5093–5097.
18. K. A. Littau, P. J. Szajowski, A. J. Muller, A. R. Kortan and L. E. Brus, *J. Phys. Chem.*, 1993, **97,** 1224–1230.
19. U. Woggon, *Optical Properties of Semiconductor Quantum Dots*, *Springer-Verlag*: Berlin, 1997.
20. C. W. Na, S. Y. Park, J. H. Chung and J. H. Lee, *ACS Appl Mater Interfaces*, 2012, **4**, 6565–6572.
21. W. B. Ingler. Jr. J. P. Baltrus, S. U. M. Khan, *J. Am. Chem. Soc.*, 2004, **126**, 10238–10239.
22. N. Ghobadi, *International Nano Lett.*, 2013, **3,** 1–5.
23. S. Uchida, Y. Yamamoto, Y. Fujishiro, A. Watanabe, O. Ito and T. Sato, *J. Mater. Chem.*, 1999, **9**, 1191-1195.
24. M. Ghosh and C.N.R. Rao, *Chem. Phys. Lett.*, 2004, **393**, 493–497.
25. G. Deepa and C. K. Mahadevan, *J. Appl. Phys.*, 2013, **5**, 15–18.
26. T. D. Schladt, T. Graf, and W. Tremel, *Chem. Mater.*, 2009, **21**, 3183–3190.
27. I. Ghada, L. L. Koleilat, S. Harnik, H. M. Stefan, S. Hinds, Andras G. P. Abraham and E. H. Sargen, *ACS Nano*, 2008, **2,** 833–840.
28. W. Zhang, X. Li, R. Zou, H. Wu, H. Shi, S. Yu and Y. Liu, *Sci. Rep.*, 2015, **5**, 11129, 1**─**9.
29. R. W. Johnston and D. C. Cronemeyer. *Phys. Rev.*, 1954, **93**, 634–635.
30. Z. Mingfei, L. Zhang, S. Limin Shao, W. Wang, F. Kangnian and Q. Qin, *J. Phys. Chem. A*, 2001, **105**, 5801–5807.
31. P. Li, C. Nan, Z. Wei, J. Lu, P. Qing and Y. Li, *Chem. Mater.*, 2010, **22**, 4232–4236.
32. M. Y. Ge, H. P. Wu, L. Niu, J. F. Liu, S. Y. Chen, P. Y. Shen, Y. W. Zeng, Y. W. Wang, G. Q. Zhang and J. Z. Jiang, *J. Cryst. Growth*, 2007, **305**, 162–166.

33. A. Giri, N. Goswami, M. Pal, M. Tay, Z. Myint, S. Al-Harthi, A. Singha, B. Ghosh, J. Dutta and S. K. Pal, *J. Mater. Chem. C*, 2013, **1**, 1885–1895.
34. M. Y. Ge, H. P. Wu, L. Niu, J. F. Liu, S. Y. Chen, P. Y. Shen, Y. W. Zeng, Y. W. Wang, G. Q. Zhang and J. Z. Jiang, *J. Cryst. Growth*, 2007, **305**, 162–166.
35. J. W. Lee, A. S. Hall, J.-D. Kim and T. E. Mallouk, *Chem. Mater.*, 2012, **24**, 1158–1164.
36. N. Thovhogi, E. Park, E. Manikandan, M. Maaza, and A. Gurib-Fakim, *J. Alloys Compounds*, 2016, **655**, 314–320.
37. H. Huang, S. Sithambaram, C.-H. Chen, C. King'ondu Kithongo, L. Xu, A. Iyer, H. F. Garces and S.L. Suib, *Chem. Mater.*, 2010, **22**, 3664−3669.
38. J. Chen, X. Tang, J. Liu, E. Zhan, J. Li, X. Huang and W. Shen, *Chem. Mater*., 2007, **19**, 4292−4299.
39. S. C. Erwin, L. Zu, M. I. Haftel, A. L. Efros, T. A. Kennedy and D. J. Norris, *Nature*, 2005, **436**, 91–94.
40. J. Tauc R. Grigorovici and A. Vancu, *Phys. Status Solidi*, 1966, **15,** 627–637.
41. S. K. Dutta, S. K. Mehetor and N. Pradhan, *J. Phys. Chem. Lett.*, 2015, **6**, 936−944.
42. Z. L. Wang, *Appl. Phys. A: Mater. Sci. Process*., 2007, **88**, 7–15.
43. M. Y. Berezin In *Nanotechnology for Biomedical Imaging and Diagnostics: From Nanoparticle Design to Clinical Applications*, Wiley Interscience, New York, 2014. 312–313.
44. V. S. Antonin, S. Garcia-Segura, M. C. Santos and E. Brillas, *J. Electroanal. Chem.*, 2015, **747**,1–11.